

Journal of Biomedical Optics

SPIDigitalLibrary.org/jbo

Single myelin fiber imaging in living rodents without labeling by deep optical coherence microscopy

Juliette Ben Arous
Jonas Binding
Jean-François Léger
Mariano Casado
Piotr Topilko
Sylvain Gigan
A. Claude Boccara
Laurent Bourdieu

Single myelin fiber imaging in living rodents without labeling by deep optical coherence microscopy

Juliette Ben Arous,^{a,b,c,*} Jonas Binding,^{a,b,c,d,e,f,*} Jean-François Léger,^{a,b,c} Mariano Casado,^{a,b,c} Piotr Topilko,^{a,b,c} Sylvain Gigan,^d A. Claude Boccard,^d and Laurent Bourdieu^{a,b,c}

^aEcole Normale Supérieure, Institut de Biologie de l'ENS, IBENS 46 rue d'Ulm, Paris, 75005 France

^bInserm, U1024, Paris, 75005 France

^cCNRS, UMR 8197, Paris, 75005 France

^dInstitut Langevin, UMR7587 CNRS, ESPCI, 10 rue Vauquelin, Paris, 75005 France

^eMax Planck Institute for Medical Research, Jahnstraße 29, 69120 Heidelberg, Germany

^fFondation Pierre-Gilles de Gennes pour la Recherche, 29 rue d'Ulm, Paris, 75005 France

Abstract. Myelin sheath disruption is responsible for multiple neuropathies in the central and peripheral nervous system. Myelin imaging has thus become an important diagnosis tool. However, *in vivo* imaging has been limited to either low-resolution techniques unable to resolve individual fibers or to low-penetration imaging of single fibers, which cannot provide quantitative information about large volumes of tissue, as required for diagnostic purposes. Here, we perform myelin imaging without labeling and at micron-scale resolution with $>300\text{-}\mu\text{m}$ penetration depth on living rodents. This was achieved with a prototype [termed deep optical coherence microscopy (deep-OCM)] of a high-numerical aperture infrared full-field optical coherence microscope, which includes aberration correction for the compensation of refractive index mismatch and high-frame-rate interferometric measurements. We were able to measure the density of individual myelinated fibers in the rat cortex over a large volume of gray matter. In the peripheral nervous system, deep-OCM allows, after minor surgery, *in situ* imaging of single myelinated fibers over a large fraction of the sciatic nerve. This allows quantitative comparison of normal and *Krox20* mutant mice, in which myelination in the peripheral nervous system is impaired. This opens promising perspectives for myelin chronic imaging in demyelinating diseases and for minimally invasive medical diagnosis.

© 2011 Society of Photo-Optical Instrumentation Engineers (SPIE). [DOI: 10.1117/1.3650770]

Keywords: myelin; full-field optical coherence tomography; endogenous contrast; optical aberrations; live imaging.

Paper 11285R received Jun. 7, 2011; revised manuscript received Aug. 3, 2011; accepted for publication Sep. 20, 2011; published online Oct. 31, 2011; corrected Nov. 4, 2011.

1 Introduction

The myelin sheath is an essential component of the vertebrate nervous system composed of glial membrane layers tightly wrapped around axonal fibers. Its high lipid content allows electrical insulation of the axonal membrane and enables saltatory conduction over long distances ensuring rapid, reliable, and energetically efficient conduction of action potentials. Disruption of the myelin sheath is involved in central nervous system pathologies, such as multiple sclerosis and leukodystrophies, and peripheral nervous system (PNS) neuropathies, such as Charcot-Marie-Tooth disease.^{1,2}

Quantitative myelin imaging is a necessary tool to follow demyelination or to evaluate eventual remyelinating treatments. Myelin in the white matter can be visualized *in vitro* and *in vivo* with magnetic resonance imaging, positron emission tomography, and near-infrared imaging with a (0.1–1)-mm resolution.^{3–6} This resolution is insufficient to detect single myelinated axons, thus preventing the study of demyelination in gray matter, where myelinated fibers are sparsely organized. However demyelinating lesions in the gray matter are known to be an important hallmark of pathologies such as multiple sclerosis.⁷

Different approaches have been recently designed to overcome this limitation. Coherent anti-Stokes–Raman scattering microscopy allows the visualization of single fibers without exogenous labeling.^{8,9} This technique has a penetration depth of only a few tens of micrometers and cannot provide quantitative information on large volumes of nervous tissue. Third harmonic generation provides signals from myelin¹⁰ with an improved penetration but is still a costly and complicated technique, and its use for *in vivo* recording in the cortex has not yet been demonstrated. A noninvasive method allowing imaging of myelin with individual fiber resolution is therefore still lacking.

Optical coherence tomography (OCT) is a simple yet powerful technique based on interference that allows noninvasive imaging of biological samples and provides optical sectioning deep into scattering tissues.^{11,12} Full-field OCT (ff-OCT) is a high spatial resolution version of OCT, the only providing micron resolution in three dimensions.¹³ OCT uses the backscattered light due to refractive index (n) variations in the sample as a source of endogenous contrast. The lipid-rich myelin sheath has a high refractive index (up to $n \sim 1.455 \pm 0.015$ in the visible¹⁴) and lies in an aqueous background ($n \sim 1.33$ in the visible¹⁵). Here we show that myelin produces a strong endogenous backscattering signal. To take advantage of this signal, we have designed a prototype of a high-numerical aperture infrared ff-OCT microscope with automatic correction of defocus

*These authors contributed equally to this work.

Address all correspondence to: Laurent Bourdieu, Ecole Normale Supérieure, Institut de Biologie de l'ENS, IBENS 46 rue d'Ulm, Paris, F-75005 France. Tel: +33 144323734; Fax: +33 144323887; E-mail: laurent.bourdieu@ens.fr.

aberration.^{16,17} This prototype, designated as deep-OCM, allows high-resolution myelin imaging deep in tissue without staining. We present two applications of myelin imaging in large volumes of tissue with single fiber resolution: the myelination of individual fibers during development in the rat cortex and the comparison of sciatic nerve structure in wild-type and mutant mice in which myelination in the PNS is impaired.

2 Materials and Methods

2.1 Animals

All animal manipulation and surgical procedures were in accordance with the European Community guidelines on the care and use of animals,¹⁸ French legislation,¹⁹ and the recommendations of the CNRS. Male Wistar rats, female Swiss CNP-EGFP mice²⁰ [cyclic nucleotide phosphodiesterase (CNP)], C57BL/6/DBA2 wild-type, and *Krox20*^{-/-} mice^{21,22} were used in this study. The age of the animals used in the different experiments is specified in the next paragraphs.

2.2 Slice Preparation

For *in vivo* fixation, animals were deeply anesthetized with urethane (1.5 g/kg) and perfused transcardially with cold phosphate buffer solution (PBS) followed by 4% paraformaldehyde in PBS solution. In the somato-sensory cortex of rats (P19 and P85) and CNP-EGFP mice (P120), 100 μm thick slices were cut tangentially to the flattened cortical surface. In the cerebellum of a P19 rat, 300- μm thick sagittal slices were cut. All slices were stored in PBS before imaging. For myelin immunofluorescence labeling, after bleaching (10% H₂O₂, 13.3% Dimethyl sulfoxide, 53.3% methanol), cortical slices were incubated with rat monoclonal anti-myelin basic protein (MBP) antibodies (1:100, Millipore Bioscience Research, Billerica, MA) followed by goat anti-rat Cy3 secondary antibodies (1:500, Jackson Immuno Research, Newmarket, UK). All fluorescence images were acquired using a Leica SP2 confocal microscope (Leica Microsystems GmbH, Wetzlar, Germany) with a 10 \times objective.

2.3 Sciatic Nerve Preparation

For *in vitro* imaging, the sciatic nerves of two mice (wild-type and *Krox20*^{-/-} mutant, P14) were extracted and laid on glass slides in PBS for immediate imaging. The nerves were not held by a coverslip to prevent them from being crushed. For *in vivo* imaging, a wild-type mouse (P60) was anesthetized with ketamine (100 mg/kg) and xylazine (10 mg/kg). A small incision was performed in the left hind limb and the sciatic nerve was exposed. A plastic holder was slipped under the nerve to maintain it and prevent movements. Imaging was performed in PBS without coverslip.

2.4 Surgical Procedure for In Vivo Cortex Imaging

Three three-week old (P20-21; weight \sim 80 g), three six-week old (P45-46; weight \sim 250 g), and two 12-week old (P86-87; weight \sim 400 g) male Wistar rats were used for *in vivo* somato-sensory cortex imaging. Rats were anesthetized by urethane injection (1.5 g/kg). Supplementary doses of urethane were applied when necessary. The body temperature of the animal was held at 38 °C on a heating blanket during the whole experiment. Animals were maintained in a stereotaxic frame during the sur-

gical procedure. A craniotomy (\sim 3 mm diameter) centered on the somato-sensory cortex was performed on the rat's left hemisphere. In some cases, the dura mater was removed, as indicated in the figure legends. The craniotomy was sealed with a coverslip with 5 mm diameter that was glued onto the thinned skull to be in close contact with the brain, in order to prevent brain movements during the imaging procedure. For ff-OCT imaging, the animal was maintained with a metal holder glued on its skull to ensure optical stability. At the end of the experiments, rats were injected with a lethal dose of urethane.

2.5 Deep Optical Coherence Microscopy Setup

The microscope [Fig. 1(a)] consists of a low spatial and temporal coherence light source (250-W halogen lamp) with the standard Köhler microscope illumination, a Linnik interferometer (i.e., a Michelson interferometer with an objective in each arm), a tube lens, and a camera. The water immersion objectives used were either Zeiss IR-Achroplan 40 \times /0.8 W (to maximize lateral resolution) or Olympus UMPlanF 10 \times /0.3 W (for the observation of large fields of view). For dispersion correction, a coverslip identical to the one used to cover the sample was placed in the reference arm. To avoid the backreflection from the coverslip on the camera, the former was slightly tilted. A 50-cm doublet was used as a tube lens to image the sample and the reference arm mirror onto the camera.

Two different cameras were used: an infrared InGaAs camera (Xeva-1.7-320, Xenics Infrared Solutions, Leuven, Belgium) and a silicon camera (Pantera 1M60, Dalsa, Waterloo, Canada). Myelin fibers were detected with both sensors. Deep-OCM images taken with the InGaAs camera are noted as "IR" in the text (wavelength range 1000–1170 nm, measured at half the peak height), whereas images from the silicon camera are described as deep-red (wavelength range 700–850 nm). Deep-red imaging maximized the lateral resolution, whereas IR imaging increased further the depth penetration due to decreased scattering at longer wavelengths.²³ The InGaAs sensor chip had 320 \times 256 pixels (pixel size: 30 μm) and the silicon chip had 1024 \times 1024 pixels (pixel size: 12 μm).

Fast (\sim 30 Hz) image acquisition was performed in both cases to prevent motion artifacts and loss of contrast due to sample motion. The InGaAs and silicon cameras were operated at 66 and 57 Hz, respectively, triggered by a NI 6722 digital I/O board (National Instruments, Austin, Texas) controlled by the software Light-CT (LLTech, Paris). A synchronized rectangular 33 or 28.5 Hz signal drove the piezo linear stage actuator (PI P-753.11C, Physik Instrumente GmbH, Karlsruhe, Germany) onto which the reference arm mirror was mounted. The piezoactuator amplitude was adapted to produce a change in reference arm length of $\lambda/2$, so that the relative phase between both arms of the interferometer would change by π . Taking the difference of subsequent camera images would therefore separate the interference signal from the background light, implementing a two-step phase-stepping protocol. The software Light-CT (LLTech, Paris, France) running on a standard PC allowed real-time display of the infrared images at 33 Hz, while the higher pixel number of the silicon camera limited display speed to \sim 15 Hz. *In vivo* images were taken with the IR camera without any averaging to profit from the 30-ms exposure time. When imaging mechanically stable samples, such as tissue slices, 30 images

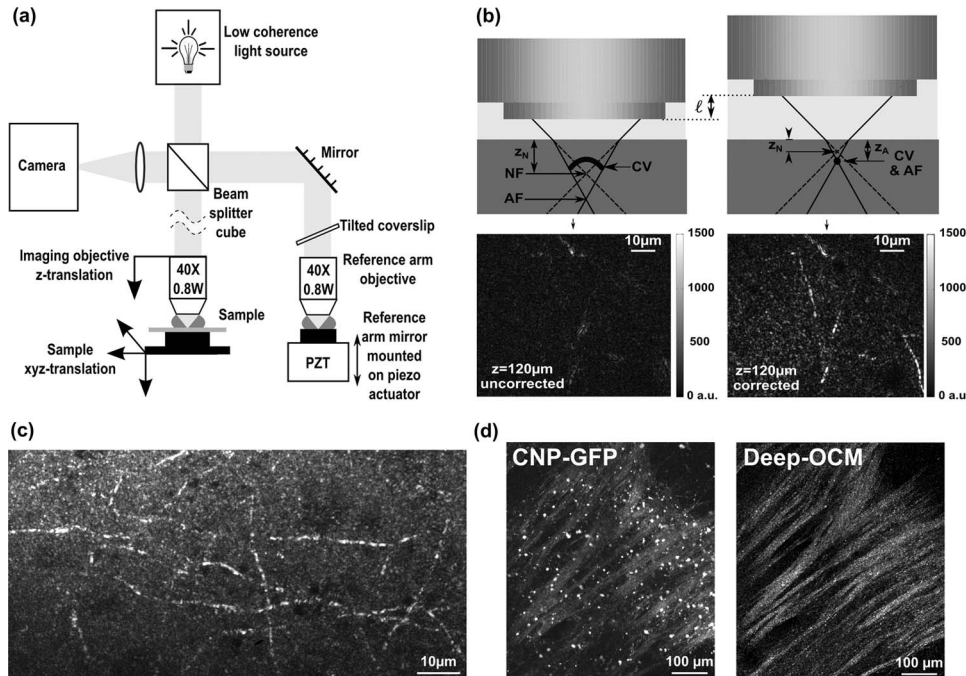


Fig. 1 Deep-OCM myelin imaging. (a) Deep-OCM setup incorporating IR and deep-red illumination, high NA objectives, compensation for defocus due refractive index mismatch, and high-speed camera. (b) Impact of index mismatch correction for OCT imaging in brain tissues. Left: In an index-matched sample, focus and coherence volume would coincide at the nominal focus (NF). Refractive index mismatch shifts the actual focus (AF) and the coherence volume (CV) away from NF so that ff-OCT images are blurred. Right: After correction, AF and CV coincide, which provides high-resolution and highly contrasted images. The images shown below the schemes are 40 \times IR deep-OCM *in vivo* images of myelin fibers in the somato-sensory cortex of a six-week-old rat ($z = 120 \mu\text{m}$ below the surface of the tissue, after removal of the dura). Left: uncorrected image; right: corrected image, defocus correction $d = 6.5 \mu\text{m}$; 30-ms exposure time. (c) Maximum projection of 40 \times deep-red deep-OCM image stack in a cortex slice (80 images taken in 0.4- μm z steps, $z = 250 \mu\text{m}$ below the brain surface; total exposure time 84 s) and stitched 10 \times IR deep-OCM images (right; maximum z projection of 3 \times 2 stitch in 100 depths, i.e., 600 images, 9-min exposure time) of the same slice of corpus callosum of a CNP-EGFP mouse. CNP-EGFP is expressed specifically in oligodendrocytes. In CNP-EGFP fluorescence images, the oligodendrocytes' cellular bodies and the myelin sheath are visible, whereas only myelin appears in deep-OCM images.

were often averaged to improve the signal-to-noise ratio, leading to per-frame exposure times of 1.05 and 0.9 s for deep-red and IR images, respectively. Both the sample z position and the relative arm length could be changed with two motorized linear stages (M-VP-25XA, Newport, Irvine, CA).

With this setup, the axial resolution (sectioning ability) is mainly due to the coherence length of the source, whereas the lateral resolution is due to the numerical aperture (NA) of the microscope objectives. In the lowest resolution configuration, with 10 \times objectives and the InGaAs camera (peak of the effective spectrum: $\lambda_{\text{max}} = 1100 \text{ nm}$), the lateral sampling of the system was 1.07 μm , the lateral resolution in water 2.2 μm (calculated using the Rayleigh formula $0.6 \cdot \lambda_{\text{max}} / \text{NA}$), and the axial resolution in water 3.3 μm (measured as the full width at half maximum of the interferogram). In the highest-resolution configuration, with 40 \times objectives and the silicon camera ($\lambda_{\text{max}} = 770 \text{ nm}$), the lateral sampling of the system was 0.1 μm , the lateral resolution in water 0.5 μm , and the axial resolution in water 1.15 μm .

2.6 Automatic Compensation of Defocus Aberration Due to Refractive Index Mismatch

Large NA makes the setup highly sensitive to depth-dependent defocus induced by refractive index mismatch between the im-

ersion medium in the sample arm and the tissue.^{16,17} Refraction at the brain surface indeed causes the actual focus z_A of the objective to be shifted deeper into the sample with respect to the nominal focus z_N [Fig. 1(b)], whereas the coherence volume penetrates the tissue slower than the nominal focus [Fig. 1(b)].¹⁷ This spatial separation of coherence volume and actual focus results in a loss in OCT signal: even the small refractive index mismatch between immersion water and brain tissue of $\sim 2\%$ is sufficient for depth penetration not to be limited by scattering-induced exponential signal decrease, as expected from Beer-Lambert law, but by signal loss due to defocus.¹⁷

Refractive index-mismatch compensation was performed online as described previously.^{16,17} Briefly, compensation is obtained by keeping the coherence volume at constant depth inside the sample and moving the actual focus into this same position [Fig. 1(b)]. Because of the aqueous immersion (group index n_g), a movement ℓ of the sample objective away from the sample increases the (paraxial) optical path in water by $2n_g\ell$, while the optical path in air only decreases by 2ℓ . To keep the coherence volume at constant depth in the sample, a displacement ℓ of the sample objective should be therefore associated with a displacement $d(\ell) = \ell(n_g - 1)$ of the reference arm. The metric used to determine the optimal positions ℓ and $d(\ell)$ was the total image intensity.¹⁷

In the following, we systematically applied automated defocus compensation, increasing the penetration depth by typically a factor of 2.5.¹⁷ In these conditions, deep-OCM provides micrometer resolution in the three dimensions and in the depth of the tissue.

2.7 Stitching

For images with a large field of view, a prototype of an ff-OCT microscope (LLTech, Paris, France) was used. It used a 640×512 pixel InGaAs Xenics Xeva camera, Olympus UPlanF $10\times/0.3W$ objectives, and a Märzhäuser xy -translation stage (Märzhäuser Wetzlar GmbH & Co. KG, Wetzlar, Germany). Stitching of individual images with 20% overlap was performed using the ImageJ plugin “Stitch Image Collection” (Stephan Preibisch, Max Planck Institute of Molecular Cell Biology and Genetics, Dresden, Germany).

2.8 Quantification

For myelin quantification, vertical stacks of images were acquired in confocal immunofluorescence and in deep-OCM (both *in vitro* and *in vivo*). The stacks had a total depth of 60–90 μm and were acquired either just below the brain surface (*in vivo*) or in the first tangential slice from the brain surface (*in vitro*). The total length of myelin filaments per unitary surface was computed as follows. The length of myelin fibers contained within the depth of field in each independent frame was first measured manually using ImageJ. The average and standard error of the mean of fiber length density per unitary surface was then calculated for 23–37 frames chosen in at least four different stacks in each imaging condition. Images from stacks obtained in rats of a given age were pooled together. Frame sizes were $120 \times 120 \mu\text{m}$ (immunofluorescence confocal), $105 \times 105 \mu\text{m}$ (*in vitro* $40\times$ deep-red deep-OCM) and $79 \times 63 \mu\text{m}$ (*in vivo* $40\times$ IR deep-OCM). The volume density of fiber length was obtained from the surface density by taking into account the thickness of each optical section (5.6 μm in confocal microscopy, 1.15 μm in *in vitro* deep-OCM, and 3.3 μm in *in vivo* deep-OCM).

Fiber diameters, lengths, and interfringe spacings were determined manually using the ImageJ Plot Profile tool. Fiber inclination A was calculated from the fibers' apparent length L via $\tan(A) = L/l_z$, where l_z is defined as the full width of the interferogram measured at 10% of the maximum ($l_z = 2.3 \mu\text{m}$ for $40\times$ deep-red deep-OCM). Statistical comparisons were performed by standard Student's t-tests.

3 Results

3.1 In Vitro Imaging of Individual Myelinated Fibers

Using deep-OCM, we were able to observe fibers in the rodent brain tissue. They show up with very high endogenous contrast due to backscattering of the incident light [Figs. 1(b) and 1(c)]. Compensation of index-mismatch-induced defocus was mandatory to observe the fibers with high contrast and resolution [Fig. 1(b)]. In $40\times$ deep-red images of rat cortical slices [Fig. 1(c)], the observed diameter of the fibers was $0.6 \pm 0.1 \mu\text{m}$ and was therefore at the diffraction limit (microscope lateral resolution: 0.56 μm), in good agreement with the diameter of individual myelinated fibers in the rat brain.²⁴

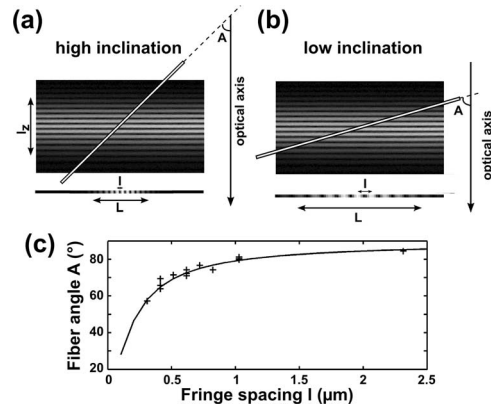


Fig. 2 Interferometric measurement of the inclination of myelinated fibers. (a, b) In deep-OCM images, the visible length L of the fiber within the coherence-gated optical section corresponds to an inclination A of the fiber and, therefore, to a fringe spacing I on the camera. (c) In $40\times$ deep-red deep-OCM images in the white matter of cerebellum slices, the inclination of fibers A , calculated from the measurement of their visible length L (see Sec. 2) corresponds to the theoretically predicted angle for a given fringe spacing I . Measuring the fringe spacing on a fiber in a 2-D image therefore provides an estimate of its inclination with respect to the optical axis.

Note that these fibers appear discontinuous in the images [see, for instance, Fig. 1(c)]. Three reasons could explain these discontinuities: (i) structural disruptions of the fiber, (ii) speckled aspect of the deep-OCM images, (iii) interference fringes along the fiber's length due to interferences with the mirror in the reference arm. Indeed, two plane waves give interference fringes, with a fringe period directly proportional to the sine of the angle between the two plane waves. In this third case, the inclination A of the fiber relative to the imaging plane should be related to the fringe period I [Figs. 2(a) and 2(b)]. The inclination of the fiber can be estimated from its total visible length L over the coherence volume thickness l_z (see Sec. 2). We show in Fig. 2(c) that fringe period I and inclination A are indeed related. Therefore, the discontinuous appearance of the fibers does not have a structural origin, and the fringe spacing allows a quantitative determination of the local fiber inclination. Imaging protocols such as four-phase imaging¹³ (instead of the two-phase imaging carried out here) should suppress this effect at the cost of slower frame rates, which makes it less appropriate for *in vivo* imaging.

To confirm that the observed fibers were myelinated axons, we compared deep-OCM and confocal fluorescence images of fiber bundles in the same slice of the corpus callosum of a mouse expressing the enhanced green fluorescent protein (EGFP) under the control of the 2'-3'-cyclic nucleotide 3'-phosphodiesterase (CNP) promoter, which causes specific labeling of oligodendrocytes. We observed the same myelin bundles in both images, whereas the cellular bodies of oligodendrocytes were only visible in the fluorescence image [Fig. 1(d)].

In order to quantify the proportion of myelinated fibers detected by deep-OCM imaging, $40\times$ deep-red images of a fixed rat horizontal cortical slice [Fig. 3(b)] were compared to confocal images of another cortical slice of the same animal where the myelin basic protein MBP had been immunostained [Fig. 3(a)]. This quantization was performed for rats of two different ages (P19 and P85). The fiber densities measured with

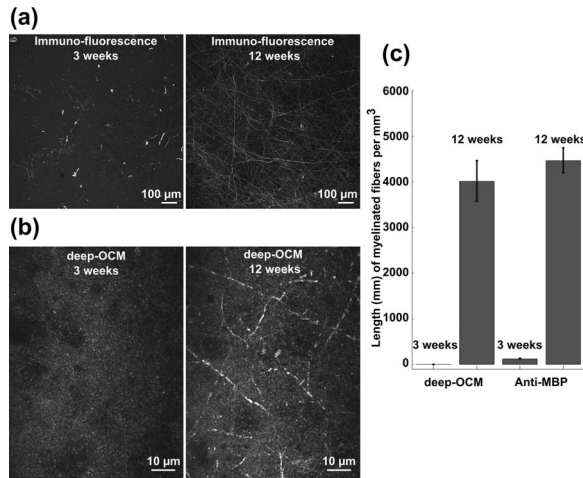


Fig. 3 *In vitro* deep-OCM imaging and quantification in the rat somato-sensory cortex. (a) Maximum projection of 10× confocal immuno-fluorescence images (anti-MBP, myelin basic protein) of tangential slices of rat somato-sensory cortex (1 mm × 1 mm × 60 μm, z = 150 μm below the brain surface; 32 images, total acquisition time around 4 min) from a P19 and a P85 rat. (b) Maximum projections of 40× deep-red deep-OCM image stacks in adjacent cortex slices (z = 250 μm) from the same animals (70 × 90 × 60 μm; 150 images, total exposure time around 3 min) as in (a). (c) Fiber length density (unit: millimeters of fiber/cubic millimeter of tissue) measured *in vitro* in tangential slices of rat somato-sensory cortex, by 40× deep-red deep-OCM and by confocal immuno-fluorescence, for 3- and 12-week-old animals. Error bars are the standard error of the mean.

the two different methods were not significantly different for 12-week-old animals [Student's *t*-test, $P = 0.39$, Fig. 3(c)]. In the case of three-week-old animals, no fibers were detected by deep-OCM imaging, whereas a very small number could be detected after immunostaining (~3% of the fiber density in adults). These few patchy myelinated zones may have been missed due to the smaller field of view of the deep-OCM images. These results indicate that this technique can be used for a quantitative analysis of myelinated axons.

Myelinated fibers could also be detected by deep-OCM in other brain structures over large fields of view. We reconstructed a complete image of a fixed rat cerebellum sagittal slice with micron resolution by stitching consecutive fields of view [10× IR, 8 × 8 mm, Fig. 4(a)]. The stereotyped organization of the cerebellar cortex allows unequivocal identification of the different structures. Because of its rich myelin content, the white matter was the most visible structure in the cerebellum. The molecular and granular layers appeared clearly distinct, and the Purkinje cell somata were visible as hollow structures [Fig. 4(c)]. Individual myelinated fibers could be readily observed in the cerebellar white matter [Fig. 4(d)], beyond the depth sectioning ability of standard bright-field microscopy. In fact, a small *z* projection of deep-OCM images [Fig. 4(b)] is necessary to visualize the full length of fibers, which can be followed from one image frame to the next in 3-D stacks of deep-OCM images (Video 1).

Myelin imaging was also performed in the peripheral nervous system. Deep-OCM 3-D reconstruction was used to obtain the structure of an acutely dissected mouse sciatic nerve *in vitro*, in which individual myelinated fibers could be discriminated [Fig. 5(a), Video 2]. Deep-OCM imaging allows optical reconstruction of a large fraction (about one-half) of the whole nerve

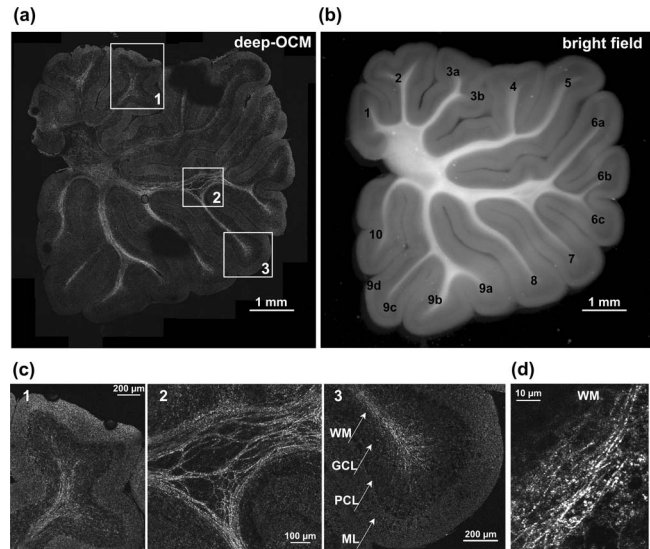
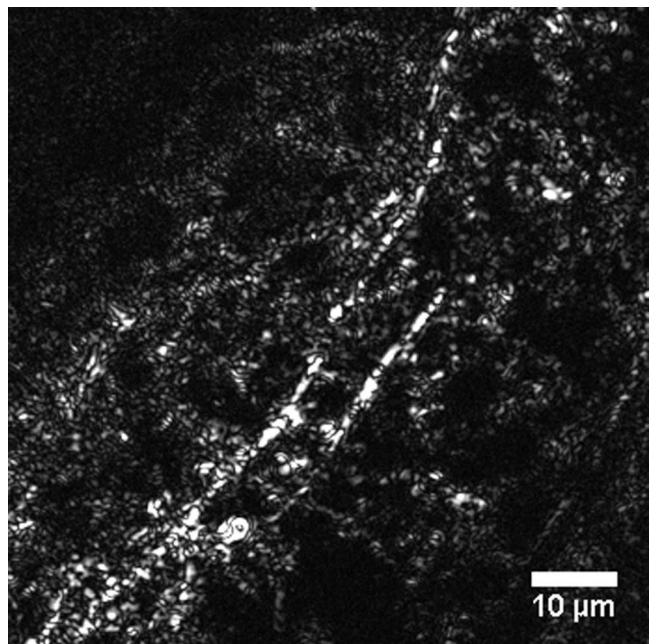


Fig. 4 High-resolution deep-OCM imaging of rat cerebellar slices. (a) 10× IR deep-OCM image of a fixed sagittal slice of a three-week-old rat; stitch of 15 × 19 = 285 images, total exposure time 11 min 24 s. (b) Bright-field low-resolution image with indication of the different cerebellar lobules. (c) Detail of the three regions delimited in A. WM: white matter; GCL: granule cell layer; PCL: Purkinje cell layer; ML: molecular layer. (d) 40× deep-red deep-OCM images of cerebellar white matter (maximum *z* projection over six images taken in 1-μm steps, total exposure time 6.3 s, corresponding to part of the volume shown in Video 1).

[Fig. 5(a)] with micrometer resolution. In order to check our ability to evaluate pathological demyelinating situations, we imaged the sciatic nerves of *Krox20* mutant mice. *Krox20* is a transcription factor whose inactivation in Schwann cells results in impaired myelination of the PNS.^{21,22} We observed a



Video 1 *In vitro* 40× deep-red deep-OCM image stack of rat cerebellar white matter (75 × 75 × 40 μm, 40 images taken in 1-μm steps, total exposure time 42 s, rescaled by 0.5 for a final voxel size of 0.2 × 0.2 × 1 μm). [URL: <http://dx.doi.org/10.1117/1.3650770.1>]

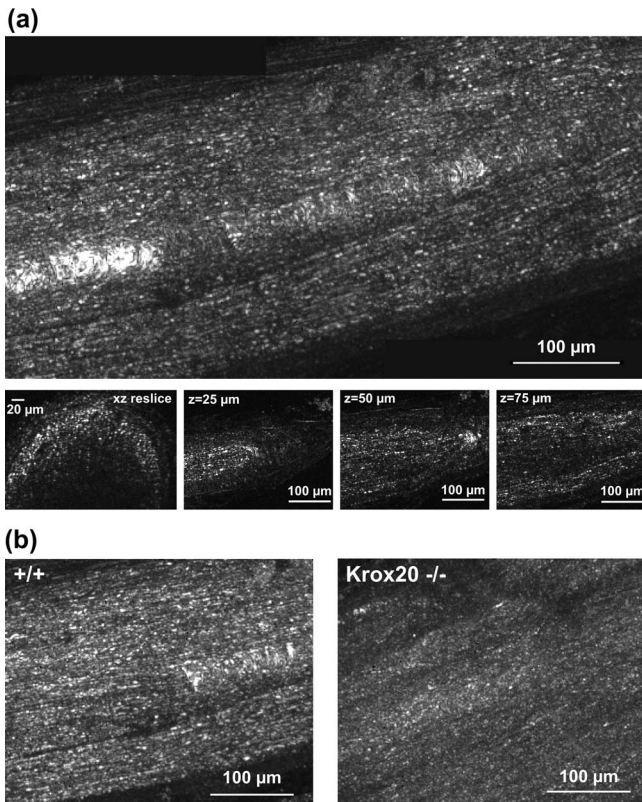


Fig. 5 *In vitro* mouse sciatic nerve imaging. (a) 10× IR deep-OCM image of an acute mouse sciatic nerve. Stitch of the maximum projections of two vertical stacks (2×200 images taken in $1\text{-}\mu\text{m}$ steps, total exposure time 6 min); the bright central zone on the left corresponds to a strong reflection on the upper surface of the nerve. Inserts, from left to right: x-z reslice of the stack and individual images 25, 50 and 75 μm deep into the nerve. (b) Comparison of a wild-type mouse nerve (left) and a *Krox20*^{-/-} mutant nerve (right). In both cases, maximum projection of a vertical stack of 10× IR deep-OCM images (500 images taken in $0.4\text{-}\mu\text{m}$ steps, total exposure time 15 min).

strong difference between nerves of *Krox20* mutant and wild-type mice [Fig. 5(b)]. Indeed, individual fibers could not be discriminated in mutant animals. Moreover, in identical imaging conditions, the reflected light amplitude was $\sim 40\%$ stronger in wild-type nerves than in mutant nerves. Thus, deep-OCM can be used to evaluate pathological myelin alteration in peripheral nerves.

3.2 *In Vivo* Imaging of Individual Myelinated Fibers

We tested whether sciatic nerve deep-OCM imaging could be performed *in vivo* in an anesthetized wild-type mouse, using minimal surgery to expose the nerve and stabilize it [Fig. 6(a)]. This was necessary to prevent respiratory or heart beat movements. *In vitro* and *in vivo* images were of comparable quality [Fig. 6(b) versus 5(a)].

Finally, we performed *in vivo* deep-OCM myelin imaging in the somato-sensory cortex of anesthetized rats. The animals were maintained in the imaging system by a tight head fixation to prevent movement during image acquisition [Fig. 7(a)]. The use of IR imaging and of refractive index–mismatch correction is particularly important in deep *in vivo* imaging, where they considerably improve the contrast and resolution of images.

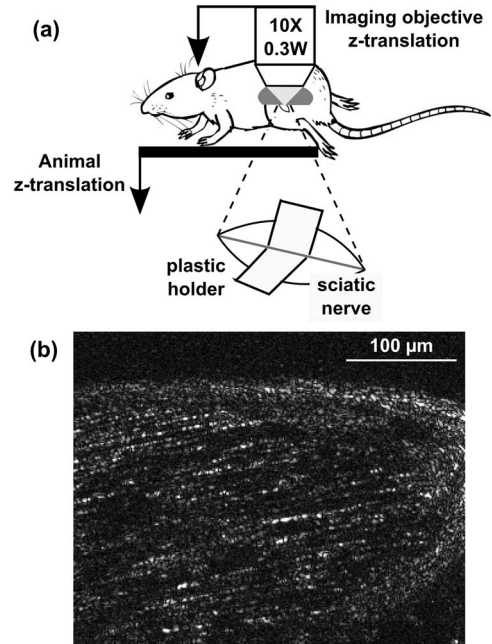
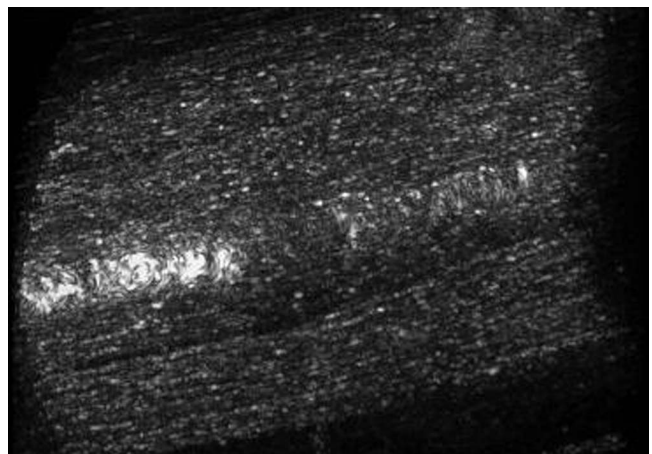


Fig. 6 *In vivo* deep-OCM myelin imaging in the mouse sciatic nerve. (a) Animal preparation. (b) *In vivo* 10× IR deep-OCM image of the sciatic nerve of a wild-type mouse ($z = 50\ \mu\text{m}$ below the surface; no averaging; exposure time 30 ms).

Two configurations were tested. In the first situation, the dura was removed, which potentially increases brain motion artifacts. In the second situation, the dura was preserved, despite its large backscattering. Detection of myelin fibers in the rat cortex was possible in both conditions [Figs. 7(b) and 7(c)].

In the absence of dura, we tested the maximum depth at which imaging could be performed. Between 10 and $640\ \mu\text{m}$ depth, four OCT images were taken every $10\ \mu\text{m}$ and then averaged. Figure 7(c) shows the normalized images at depths 20, 100, 180, 260, and $340\ \mu\text{m}$. Individual filaments could be observed up to a depth of $\sim 340\ \mu\text{m}$. Figure 7(d) shows the maximum OCT signal as a function of depth after applying a Gaussian smoothing filter



Video 2 *In vitro* 10× IR deep-OCM imaging of an acute mouse sciatic nerve. 3-D reconstruction from a $200\text{-}\mu\text{m}$ vertical stack with $0.4\text{-}\mu\text{m}$ step. The field of view is $345 \times 276\ \mu\text{m}$; 500 images, total exposure time 15 min. [URL: <http://dx.doi.org/10.1117/1.3650770.2>]

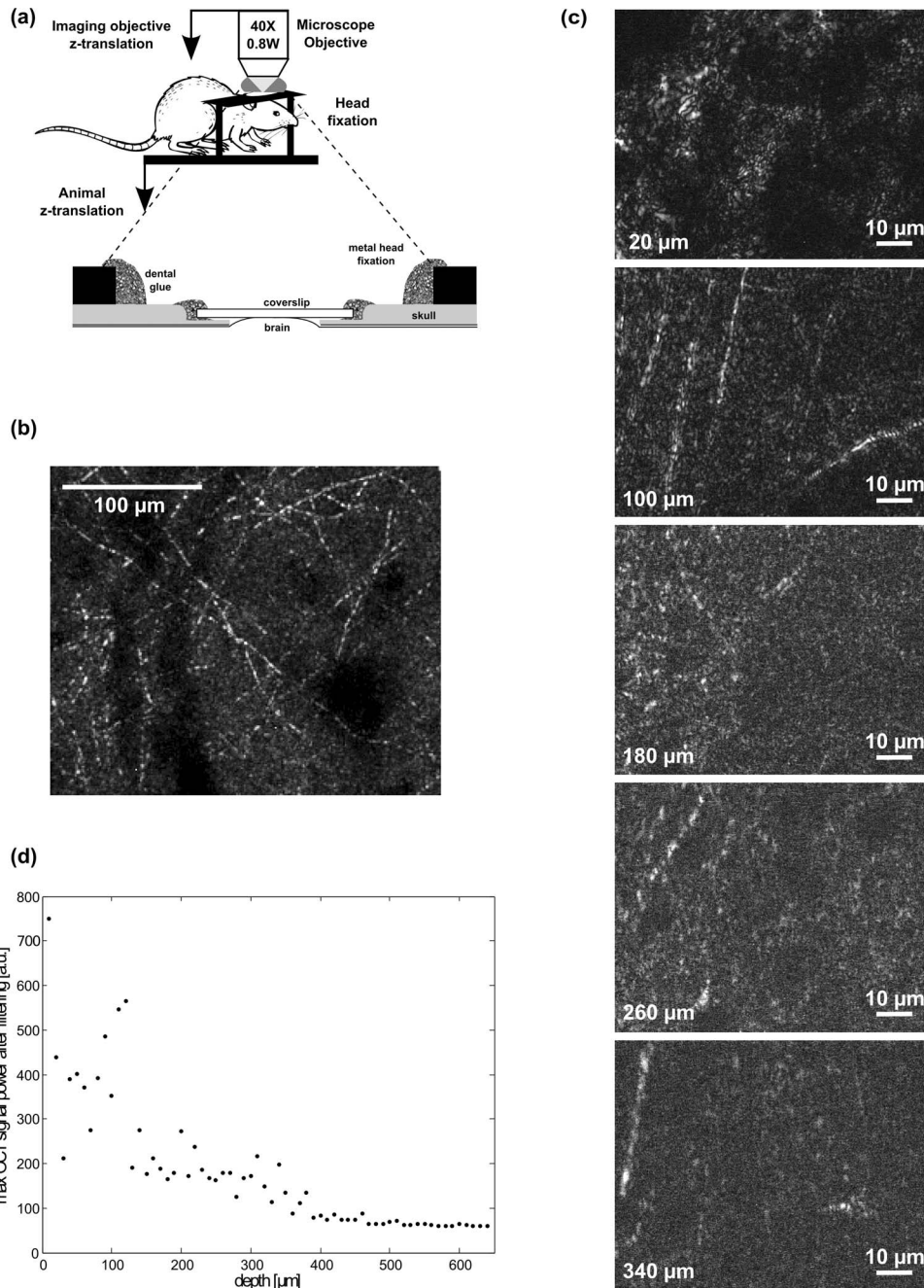


Fig. 7 *In vivo* deep-OCM myelin imaging in the rat somato-sensory cortex. (a) Animal and brain stabilization. (b) *In vivo* 10× IR deep-OCM image of the somato-sensory cortex of a six-week-old rat, under the intact dura mater. Maximum projection of a vertical stack of 200 images starting at 120 μm and ending at 140 μm below the brain surface, z step size 0.1 μm, total exposure time 12 min. (c) *In vivo* 40× IR deep-OCM images of the somato-sensory cortex of a 12-week-old rat, with the dura removed, at different depths (20, 100, 180, 260, and 340 μm); exposure time per depth was 120 ms. (d) z profile of the maximum intensity of the stack (65 images, total exposure time 7.8 s) from which the images shown in (c) were selected.

with $\sigma = 1 \mu\text{m}$ to reduce noise. Noise level is reached at depths of $>380 \mu\text{m}$, which could be either due to the sensitivity of the microscope or to the absence of horizontal myelinated fibers at this depth in cortex.

Using deep-OCM, we followed the developmental profile of myelinated fibers from 3 to 12 weeks [Figs. 8(a) and 8(b)]. Myelinated axons were observed *in vivo* up to 340 μm deep into the somato-sensory cortex of 6- and 12-week-old animals

[Fig. 8(a), middle and right], whereas no fibers were observed in the cortex of 3-week-old animals [Fig. 8(a), left]. The density of tangential fibers in the first 150 μm below the brain surface was consistent with the one measured *in vitro* [Figs. 8(b) and 3]. It was similarly high for 6- and 12-week-old rats [Student's *t*-test, $P = 0.42$, Fig. 8(b)], and was reduced in both cases at levels deeper than 150 μm, in good agreement with previous histological studies (Refs. 25–27).

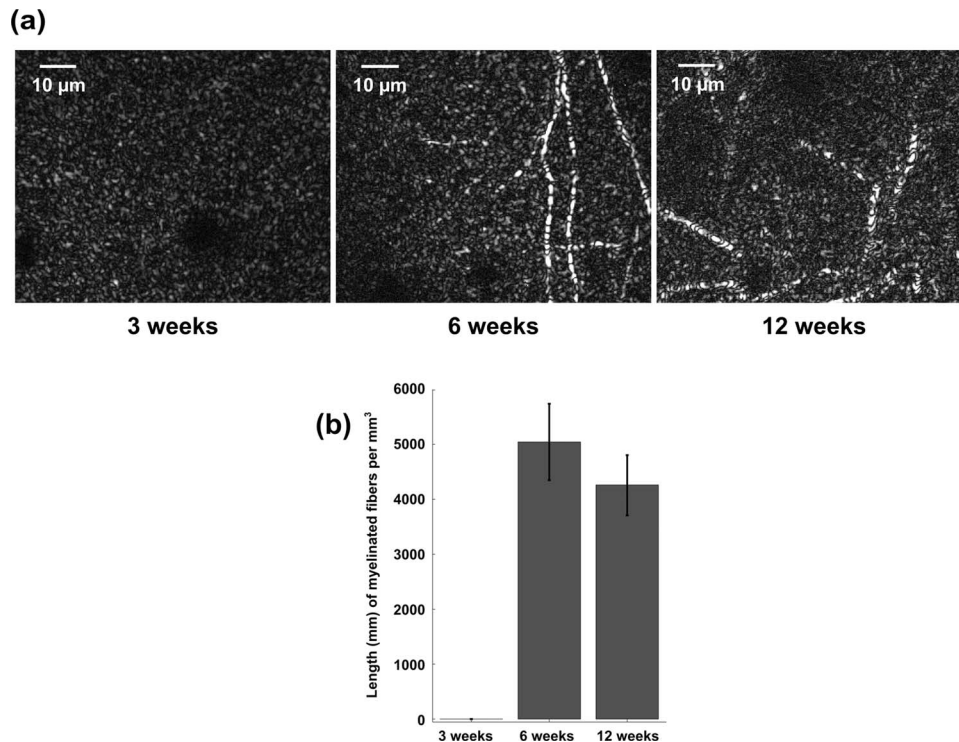


Fig. 8 Developmental profile of myelinated fibers in the cortex. (a) *In vivo* 40x IR deep-OCM images of the somato-sensory cortex of 3-week-old (left, $z = 120 \mu\text{m}$), 6-week-old (middle, $z = 120 \mu\text{m}$), and 12-week-old (right, $z = 150 \mu\text{m}$) rats (dura mater was removed in all three cases; no averaging, i.e., 30-ms exposure time each). (b) Developmental profile of the fiber length density (unit: millimeters of fiber/cubic millimeters of tissue) in the cortex. Error bars are the standard error of the mean.

4 Discussion

In this study, we have shown that deep-OCM allows quantitative imaging of individual myelinated fibers *in vitro* and *in vivo* in the rodent nervous system, with micron-size resolution, without labeling and over large volumes of tissue, up to $340 \mu\text{m}$ deep into the tissue. Deep-OCM combines several technical advances compared to standard ff-OCT microscopy, such as fast acquisition rate, IR imaging, large numerical aperture microscope objectives, and real-time defocus correction.^{16,17,23} Deep-OCM imaging of myelinated fibers benefits from their large backscattered signal. This may arise from the high local refractive index of fibers due to their high lipid content. However, whereas imaging at moderate depth was possible in a standard configuration using deep-red light, imaging at a greater depth was only possible by combining infrared detection with the correction of defocus aberration due to refractive index mismatch between immersion medium and brain tissue. Without defocus correction, both signal strength and resolution quickly degrade with depth. Finally, imaging at high temporal resolution with fast cameras in addition to a tight tissue mechanical fixation was required to avoid motion artifacts due to breathing or heart beat.

In the PNS, fast image acquisition of the myelin structure of sciatic nerves at high resolution was achieved both *in vitro* and *in vivo*, and defects of the myelin sheath observed in the raw images could be easily quantified from the reflected amplitude. Deep-OCM also allowed us to record images of individual myelinated fibers *in vivo* within the somato-sensory cortex of anesthetized rats, without exogenous labeling, and either when the dura mater was removed or directly below the intact dura

mater. Quantification of myelinated fiber density was obtained from the image analysis. Similar axonal densities have been measured in the superficial layers of the rat cortex.²⁸ By using this approach, we could observe the developmental appearance of myelin structures in the adult rat brain.

Compared to other techniques that work in this resolution and penetration depth regime, such as two-photon microscopy of genetically labeled oligodendrocytes, deep-OCM has the advantage that it directly images the local increase of refractive index caused by the high lipid content of the myelin sheath. Scanned OCM or confocal reflection microscopy (two techniques relying also on endogenous backscattering) could be similarly relevant for myelin imaging. However, confocal microscopy alone has inferior rejection of light reflected back far from the focal plane when compared to an OCT or OCM system^{29,30} and is therefore unlikely to provide comparable penetration depths. Only a combination of confocal detection with scanning OCM improves depth discrimination,^{29,30} at the expense of scanning in all three dimensions, which might make such a system prohibitively slow for *in vivo* applications. In comparison, deep-OCM is intrinsically fast as it only requires mechanical z scanning. Deep-OCM should allow extensive and even chronic imaging without the risk of signal deterioration due to bleaching, as would be the case in two-photon microscopy. Such chronic imaging of individual myelinated fibers in the upper layers of the rat cortex could be of considerable interest in neuropathies progression studies. Whole-brain imaging techniques, such as MRI, are too limited in their resolution to provide any information on the single-fiber level. Our observations open perspectives of application to chronic experiments in rodents, notably for the

longitudinal study of cortical demyelination and remyelination. To our knowledge, no other existing technique gives access to this information.

The noninvasiveness, the speed, and the depth of penetration of deep-OCM could make it a potentially interesting technique for human diagnostics. Because the access to the peripheral nervous system is quite simple and requires only minor surgery, this method may be used, in the future, in human patients with peripheral neuropathies. Deep-OCM-based myelin imaging of the sciatic nerve could replace nerve biopsy, which is a standard procedure for diagnosing certain neuropathies. It could thereby help avoid neuropathic side effects associated with nerve biopsies. More studies will be necessary to demonstrate that myelinated fibers in the PNS of human patients are as readily accessible to deep-OCM imaging as shown for rats here, and that mechanically stable recordings can be performed. Investigations of the human central nervous system with single-fiber resolution will probably require further development to attain interesting depth, for instance, using endoscopy.

In conclusion, deep-OCM makes a fine-scale analysis of the myelination processes possible, both in the cerebral cortex and in the peripheral nervous system. Such analysis currently requires time-consuming and invasive histological methods. Our technique is relatively noninvasive, affordable, and fast, and provides real-time imaging without complex off-line image treatment. It opens promising possibilities for *in vivo* acute or chronic myelin imaging as well as for the diagnosis of myelin pathologies.

Acknowledgments

We thank Marie-Stéphane Aigrot, Bruno Stankoff, and Catherine Lubetzki for their helpful comments and for transferring the transgenic CNP-GFP mice. We also thank Vittorio Gallo for authorizing us to use the mice. We thank Charles Brossollet (LLtech, Paris, France), Benjamin Mathieu, and Gaspard Gerschenfeld for their help and Shawn Mikula for critical discussions. This work was supported by ANR RIB Grants No. MICADO ANR-07-RIB-010-02 and No. ANR-07-RIB-010-04. J.B. was funded by a PhD fellowship from Fondation Pierre-Gilles de Gennes.

References

- S. S. Scherer and L. Wrabetz, "Molecular mechanisms of inherited demyelinating neuropathies," *Glia* **56**(14), 1578–1589 (2008).
- N. Baumann and D. Pham-Dinh, "Biology of oligodendrocyte and myelin in the mammalian central nervous system," *Physiol. Rev.* **81**(2), 871–927 (2001).
- C. Laule, I. M. Vavasour, S. H. Kolind, D. K. Li, T. L. Traboulsee, G. R. Moore, and A. L. MacKay, "Magnetic resonance imaging of myelin," *Neurotherapeutics* **4**(3), 460–484 (2007).
- S. Mori and J. Zhang, "Principles of diffusion tensor imaging and its applications to basic neuroscience research," *Neuron* **51**(5), 527–539 (2006).
- B. Stankoff, Y. Wang, M. Bottlaender, M. S. Aigrot, F. Dolle, C. Wu, D. Feinstein, G. F. Huang, F. Semah, C. A. Mathis, W. Klunk, R. M. Gould, C. Lubetzki, and B. Zalc, "Imaging of CNS myelin by positron-emission tomography," *Proc. Natl. Acad. Sci. U.S.A.* **103**(24), 9304–9309 (2006).
- C. Wang, C. Wu, D. C. Popescu, J. Zhu, W. B. Macklin, R. H. Miller, and Y. Wang, "Longitudinal near-infrared imaging of myelination," *J. Neurosci.* **31**(7), 2382–2390 (2011).
- J. J. Geurts, S. D. Roosaendaal, M. Calabrese, O. Ciccarelli, F. Agosta, D. T. Chard, A. Gass, E. Huerga, B. Moraal, D. Pareto, M. A. Rocca, M. P. Wattjes, T. A. Yousry, B. M. Uitdehaag, and F. Barkhof, "Consensus recommendations for MS cortical lesion scoring using double inversion recovery MRI," *Neurology* **76**(5), 418–424 (2011).
- Y. Fu, T. B. Huff, H. W. Wang, H. Wang, and J. X. Cheng, "Ex vivo and in vivo imaging of myelin fibers in mouse brain by coherent anti-Stokes Raman scattering microscopy," *Opt. Express* **16**(24), 19396–19409 (2008).
- J. Imitola, D. Cote, S. Rasmussen, X. S. Xie, Y. Liu, T. Chitnis, R. L. Sidman, C. P. Lin, and S. J. Khoury, "Multimodal coherent anti-Stokes Raman scattering microscopy reveals microglia-associated myelin and axonal dysfunction in multiple sclerosis-like lesions in mice," *J. Biomed. Opt.* **16**(2), 021109 (2011).
- M. J. Farrar, F. W. Wise, J. R. Fetcho, and C. B. Schaffer, "In vivo imaging of myelin in the vertebrate central nervous system using third harmonic generation microscopy," *Biophys. J.* **100**, 1362–1371 (2011).
- J. G. Fujimoto, "Optical coherence tomography for ultrahigh resolution in vivo imaging," *Nat. Biotechnol.* **21**(11), 1361–1367 (2003).
- J. G. Fujimoto, M. E. Brezinski, G. J. Tearney, S. A. Boppart, B. Bouma, M. R. Hee, J. F. Southern and E. A. Swanson, "Optical biopsy and imaging using optical coherence tomography," *Nat. Med.* **1**(9), 970–972 (1995).
- L. Vabre, A. Dubois, and A. C. Boccara, "Thermal-light full-field optical coherence tomography," *Opt. Lett.* **27**(7), 530–532 (2002).
- I. P. Antonov, A. V. Goroshkov, V. N. Kalyunov, I. V. Markhvida, A. S. Rubanov, and L. V. Tanin, "Measurement of the radial distribution of the refractive index of the Schwann's sheath and the axon of a myelinated nerve fiber in vivo," *J. Appl. Spectrosc.* **39**(1), 822–824 (1983).
- M. Daimon and A. Masumura, "Measurement of the refractive index of distilled water from the near-infrared region to the ultraviolet region," *Appl. Opt.* **46**(18), 3811–3820 (2007).
- S. Labiau, G. David, S. Gigan, and A. C. Boccara, "Defocus test and defocus correction in full-field optical coherence tomography," *Opt. Lett.* **34**(10), 1576–1578 (2009).
- J. Binding, J. Ben Arous, J.-F. Léger, S. Gigan, C. Boccara, and L. Bourdieu, "Brain refractive index measured in vivo with high-NA defocus-corrected full-field OCT and consequences on two-photon microscopy," *Opt. Express* **19**(6), 4833–4847 (2011).
- Directive 86/609/CEE, CE official journal L358 (December 18, 1986).
- Décret No. 97/748, 19 October, 1987, J. O. République française (October 20, 1987).
- X. Yuan, R. Chittajallu, S. Belachew, S. Anderson, C. J. McBain, and V. Gallo, "Expression of the green fluorescent protein in the oligodendrocyte lineage: a transgenic mouse for developmental and physiological studies," *J. Neurosci. Res.* **70**(4), 529–545 (2002).
- P. Topilko, S. Schneider-Maunoury, G. Levi, A. Baron-Van Evercooren, A. B. Chennoufi, T. Seitanidou, C. Babinet, and P. Charnay, "Krox-20 controls myelination in the peripheral nervous system," *Nature* **371**(6500), 796–799 (1994).
- F. Couplier, L. Decker, B. Funalot, J.-M. Vallat, F. Garcia-Bragado, P. Charnay, and P. Topilko, "CNS/PNS boundary transgression by central glia in the absence of Schwann cells or Krox20/Egr2 function," *J. Neurosci.* **30**(17), 5958–5967 (2010).
- D. Sacchet, J. Moreau, P. Georges, and A. Dubois, "Simultaneous dual-band ultra-high resolution full-field optical coherence tomography," *Opt. Express* **16**(24), 19434–19446 (2008).
- G. Partadiredja, R. Miller, and D. E. Oorschot, "The number, size, and type of axons in rat subcortical white matter on left and right sides: a stereological, ultrastructural study," *J. Neurocytol.* **32**(9), 1165–1179 (2003).
- S. Mikula, I. Trotts, J. M. Stone, and E. G. Jones, "Internet-enabled high-resolution brain mapping and virtual microscopy," *NeuroImage* **35**(1), 9–15 (2007).
- I. Trotts, S. Mikula, and E. G. Jones, "Interactive visualization of multi-resolution image stacks in 3D," *NeuroImage* **35**(3), 1038–1043 (2007).
- <http://brainmaps.org/ajax-viewer.php?datid=148&aname=07>.
- J. T. Eayrs and B. Goodhead, "Postnatal development of the cerebral cortex in the rat," *J. Anat.* **93**(Pt 4), 385–402 (1959).
- J. A. Izatt, M. R. Hee, G. M. Owen, E. A. Swanson, and J. G. Fujimoto, "Optical coherence microscopy in scattering media," *Opt. Lett.* **19**(8), 590–592 (1994).
- J. Mertz, *Introduction to Optical Microscopy*, Roberts, Greenwood Village, CO (2010).